ADVANCED FUNCTIONAL MATERIALS
www.afm-journal.de

Bionic Adaptive Thin-Membranes Sensory System Based on Microspring Effect for High-Sensitive Airflow Perception and Noncontact Manipulation

Wei Zhou, Peng Xiao, Yun Liang, Qiling Wang, Depeng Liu, Qing Yang,* Jianhua Chen, Yujing Nie, Shiao-Wei Kuo, and Tao Chen**

Recently airflow sensors based on mechanical deformation mechanisms have drawn extensive attention due to their favorable flexibility and sensitivity. However, the fabrication of highly sensitive and self-adaptive airflow sensors in a simple, controllable, and scalable method still remains a challenge. Herein, inspired by the wing membrane of a bat, a highly sensitive and adaptive graphene/single-walled nanotubes-Ecoflex membrane (GSEM) based airflow sensor mediated by the reversible microspring effect is developed. The fabricated GSEM is endowed with an ultralow airflow velocity detection limit (0.0176 m s^{-1}), a fast response time (≈1.04 s), and recovery time (≈1.28 s). The GSEM-based airflow sensor can be employed to realize noncontact manipulation. It is applied to a smart window system to realize the intelligent, open, and close behaviors via a threshold control. In addition, an array of airflow sensors is effectively designed to differentiate the magnitude and spatial distribution of the applied airflow stimulus. The GSEM-based airflow sensor is further integrated into a wireless vehicle model system, which can sensitively capture the flow velocity information to realize a real-time direction of motion manipulation. The microspring effect-based airflow sensing system shows significant potentials in the fields of wearable electronics and noncontact intelligent manipulation.

1. Introduction

In nature, creatures such as human beings and animals have complex and diverse sensory systems that can respond to mechanical, temperature, humidity, and other imperceptible external stimulus (e.g., smell, light, sound, breeze, etc.) to effectively perceive environment information.[1–8] Among them, the function of airflow perception is an important part of sensory systems that existed in creatures that can effectively respond to noncontact stimuli in uncertain environments (e.g., dark, noisy, etc.) to tackle imperceptible dangers.[9–12] Actually, in practical applications, achieving sensitive and rapid airflow sensing is urgently required due to its wide and diverse applications in breath monitoring,[13] airplane flight control,[14] weather observation,[15] mine warning,[16] etc. In recent years, extensive efforts have been devoted to developing airflow sensors to expand the field of flexible electronics.

W. Zhou, P. Xiao, Y. Liang, Q. Wang, D. Liu, T. Chen
Key Laboratory of Marine Materials and Related Technologies
Zhejiang Key Laboratory of Marine Materials and Protective Technologies
Ningbo Institute of Materials Technology and Engineering
Chinese Academy of Sciences
Ningbo 315201, China
E-mail: xiaopeng@nimte.ac.cn; tao.chen@nimte.ac.cn

W. Zhou, P. Xiao, Y. Liang, Q. Wang, D. Liu, T. Chen
School of Chemical Sciences
University of Chinese Academy of Sciences
19A Yuquan Road, Beijing 100049, China

Q. Yang
State Key Laboratory of Modern Optical Instrumentation
College of Optical Science and Engineering
International Research Center for Advanced Photonics
Zhejiang University
Hangzhou 310027, China
E-mail: qingyang@zju.edu.cn

Q. Yang
Research Center for Intelligent Sensing
Zhejiang Lab
Hangzhou 311100, China

J. Chen, Y. Nie
Fujian Province University Key Laboratory of Modern Analytical Science and Separation Technology
College of Chemistry Chemical Engineering and Environment
Minnan Normal University
Zhangzhou 363000, China

S.-W. Kuo
Department of Material and Optoelectronic Science
Center of Crystal Research
National Sun Yat-Sen University
Kaohsiung 804, Taiwan

The ORCID identification number(s) for the author(s) of this article can be found under https://doi.org/10.1002/adfm.202105323.

DOI: 10.1002/adfm.202105323

Compared with traditional rigid and bulky systems,[17–20] flexible materials enabled airflow sensors based on mechanical deformation (e.g., piezoresistive,[21–25] capacitive,[26] piezoelectric,[27,28] electrical,[29] optical,[30] and magnetic[31,32] mechanism) are endowed with features of flexibility, miniaturization, and mild operation condition. For example, the covalently assembled graphene oxide (GO) ultrathin film can experience a reversible change of interlayer gaps to reach efficient detection of airflow.[29] Besides, a carbon nanotubes based fluffy fabric can be easily sewn to clothes to sensitively capture tiny airflow fluctuation for wearable electronics.[25] However, the realization of airflow sensors with ultralow detection limit, fast response time, simple structure, and high adaptability in a facile, efficient and low-cost way still remains a challenge.

Bats have ultrasensitive airflow sensory organs on their wing membranes characterized by flexible, elastic, and thin properties to detect airflow condition for smooth flight.[33,34] In the sensory system, the fine hairs embedded in wing membranes can sensitively capture the tiny airflow variation and experience reversible mechanical bending displacement to rapidly trigger the Merkel cells (a slow adapting mechanoreceptor that responds to gentle touch) around the hair follicles, resulting in action current that is transmitted through nerve fibers to the central nervous system to percept airflow (**Figure 1**a).[35,36] The simple and effective evolved sensory structures have inspired us to design a highly sensitive and adaptive airflow sensor based on microspring effect, which is enabled by well-designed graphene/single-walled nanotubes (SWNTs)-Ecoflex membrane (GSEM). The monolithic GSEM was prepared via an air/water interfacial self-assembly and asymmetric functionalization strategy,[37–41] allowing the formation of a highly adaptive, elastic, and conductive membrane with SWNTs randomly distributed among graphene sheets for reversible microspring structures (Figure 1b). When GSEM is blown by airflow, the vertical downward wind force increases the contact points between the interlayer spring-like SWNTs and the underlying graphene sheets or SWNTs, resulting in the GSEM-based airflow sensor exhibiting current-increased sensing performance. (Figure 1b). The integrated GSEM airflow sensor represents ultralow airflow velocity detection limit (0.0176 m s^{-1}), fast response time (≈1.04 s) and recovery time (≈1.28 s), and high stability of 660 times cycles. As a result, a GSEM-enabled intelligent window system was further designed to sense the airflow velocity threshold for controllable open and close. In addition, a 4 × 4 airflow sensor

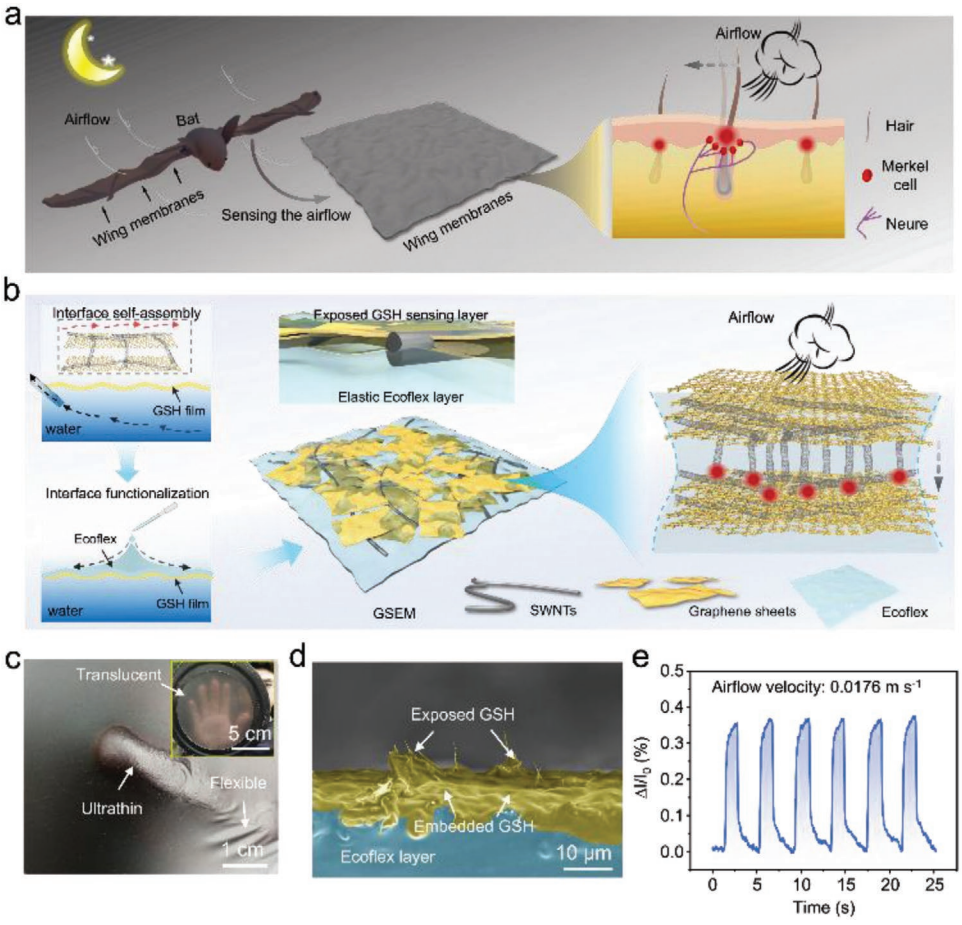

Figure 1. a) Schematic of bat's wing membrane structure and airflow perception principle. b) Diagram of the preparation, structure, and sensing principle of bionic structured GSEM for airflow sensing. c) Photograph of ultrathin GSEM with one finger closely contact under the Ecoflex surface. Inset: The outline of the human palm can be observed through GSEM. d) Cross-sectional SEM image of GSEM with obvious exposed and embedded GSH sensing layer. e) Airflow sensor based on GSEM is able to detect airflow as low as 0.0176 m s^{-1} with excellent cyclic stability.

array was constructed to effectively differentiate the magnitude and spatial distribution of applied airflow stimulus. Moreover, based on this sensor array, a wireless vehicle can be sensitively manipulated in a noncontact mode to realize a high-sensitive direction control. The microspring effect interacted flexible and adaptable membrane shows great promise in flexible electronics and noncontact intelligent devices manipulation.

2. Results and Discussion

The fabricated GSEM demonstrates ultrathin and flexible features, which can conformally adapt to the finger surface and clearly present the texture of finger skin (Figure 1c). Owing to the translucency of GSEM, the contours of a human palm can be visualized through the film in the presence of light. Note that the abovementioned properties of GSEM are quite similar to the macroscopic properties of the bat's wing membrane. Microscopically, the cross-sectional scanning electron microscopy (SEM) image of GSEM is shown in Figure 1d and Figure S1, Supporting Information, which indicates a monolithic membrane structure with graphene/SWNTs hybrid (GSH) sensing layer embedded or exposed on one side of the Ecoflex matrix, giving the membrane favorable structural combinative ability and conductivity for signal sensing. The monolithic structure is also characterized by the Raman spectrum and 2D mapping image in Figure S2, Supporting Information, which presents characteristic peaks of both graphene/SWNTs (D: 1343 cm^{-1}, G: 1587 cm^{-1}, 2D: 2684 cm^{-1}) and Ecoflex (low frequency: 488 cm^{-1}, 707 cm^{-1}; high frequency: 2904 cm^{-1}, 2962 cm^{-1}) on GSH side. The airflow sensor fabricated by transferring GSEM onto the glass slide can detect flow velocity as low as 0.0176 m s^{-1} with good repeatability (Figure 1e), demonstrating the significant potentials of this monolithic structure for airflow sensing.

Since the bionic hybrid structure of GSEM can respond rapidly and sensitively to airflow stimuli, the potential working mechanism is also studied in our system. To explore the effect of microspring microstructure, control experiments with pure 1D and 2D membranes were conducted to detect applied airflow, including assembled graphene sheets and physically entangled SWNTs network. First, cross-sectional SEM images were captured to demonstrate the initial sensing layer structures of pure graphene, GSH, and pure SWNTs films (**Figure 2**a–c). As displayed in Figure 2a, there is a lamellar stacked structure with a few tiny gaps between graphene nanosheets. In addition, the SWNTs film presents a densely entangled conductive network (Figure 2c). For the GSH sample, it can be observed that SWNTs are randomly distributed on the surface and further extends to the gaps among graphene nanosheets, forming a specific spring-like microstructure. It is expected that when

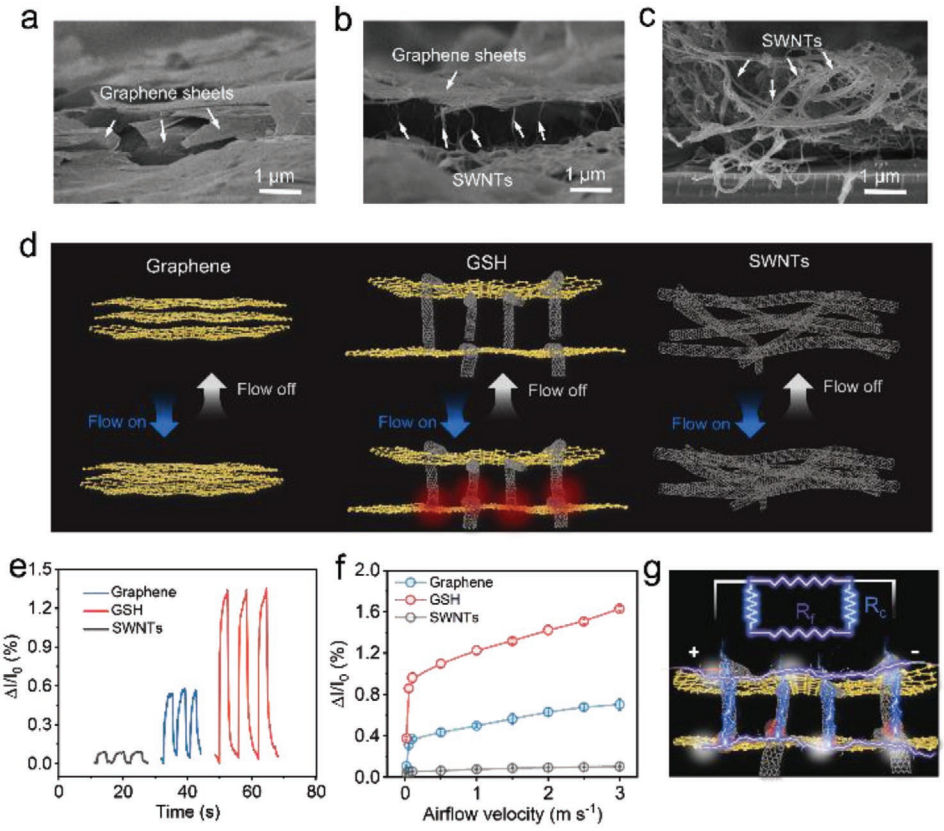

Figure 2. Cross-sectional SEM images of films based on a) pure graphene, b) GSH, and c) pure SWNTs in the initial condition without airflow. d) Schematics of changes in the internal microstructure of graphene, GSH, and SWNTs films before and after airflow being applied. e) Cyclic sensing curves of the relative current variation at the airflow velocity of 1.5 m s^{-1} and f) plots of the relative change in current versus airflow velocity of pure graphene, GSH, and pure SWNTs films. g) Diagram of the current flow and the equivalent circuit of an ideal structural unit in GSH.

the mechanical force is applied, the distance between graphene nanosheets can experience remarkable change, resulting in the sensitive change of contact resistance for excellent airflow sensing performance. Besides, the surface morphology of the above three samples is presented in Figure S3, Supporting Information, which illustrates that the assembled films are endowed with uniform microstructures. Based on the initial microstructures discussed above, schematic models are developed to further explain the enhanced performance of the hybrid system (Figure 2d). When the airflow is applied, the microspring-like SWNTs in the GSH will prominently increase the contact area with the underlying graphene sheets or SWNTs through the microscale movement or deformation of interlayer SWNTs[42–45] for remarkable reduction of contact resistance. In comparison, graphene sheets-based film and SWNTs-based one both represent a relatively slight increase of contact area. As a result, the GSH-based microspring structure enables improved performance of airflow sensing. The relative current variation curves of thin-membranes based on graphene, GSH and SWNTs sensing layers were tested at 1.5 m s^{-1} and the hybrid system is found to have the largest current variation (Figure 2e). Furthermore, Figure 2f shows a typical positive correlation relationship between relative current variation and airflow velocity, where the GSH film presents the best airflow responding performance.

A diagram of the current flow between an ideal structural unit in GSH is presented in Figure 2g. The current is mainly composed of two parts. One is the current that flows laterally, which primarily flows between graphene nanosheets, between SWNTs network, and between graphene and SWNTs. The corresponding resistance is the bulk film resistance, labeled as R_f. The other is the longitudinal current, which is mostly due to the decrease in contact resistance of the interlayered SWNTs by micro-deformation based on the microspring effect when the airflow is applied, and the related resistance is noted as R_c. The equivalent circuit of the structural unit in GSH is established based on the schematic of current flow. The total resistance R_t can be calculated according to Ohm's law, as shown in Equation (1):

$$R_t = \frac{R_f\left(2R_c + R_f\right)}{2\left(R_c + R_f\right)} = \frac{R_f}{2}\left(1 + \frac{1}{\frac{R_f}{R_c} + 1}\right) \quad (1)$$

Compared with the R_f, R_c is sensitive to airflow. Once the airflow is applied, R_c will decrease rapidly. As can be seen from Equation (1), a decrease in R_c will eventually lead to a decrease in R_t, suggesting the airflow sensing performance with an increase of current for GSEM-based airflow sensor. Furthermore, the argon response behavior of GSEM-based airflow sensor was also tested. As shown in Figure S4, Supporting Information, compared with the nitrogen, the airflow sensor exhibits almost the same sensing performance at the airflow velocity of 0.0176 m s^{-1}, which indicates that this sensor primarily detects the airflow rather than the gas type.

The effect of hybridization with different weights ratio of SWNTs and Gr on the airflow sensing performance is further discussed, as shown in **Figure 3**a. Whether G_3S_1H or G_1S_3H film, hybridization can dramatically improve airflow responsiveness compared to pure graphene sheets or SWNTs as discussed in Figure 2. However, the sensing performance of films with G_3S_1H and G_1S_3H as sensing layers is slightly inferior compared with that of G_1S_1EM, which may result from the failure of forming microstructures with the optimal number and uniform distribution in G_3S_1EM and G_1S_3EM. As shown in Figure S4a,d, Supporting Information, SWNTs in G_3S_1H are sparsely distributed on the surface of the graphene sheets, and only a small amount of SWNTs formed a microspring-like support structure between the graphene sheets. When the airflow blows onto the surface of the membrane, the scarce interlayered SWNTs lead to a small change in contact resistance. In G_1S_3H, excessive SWNTs aggregated to form carbon nanotube bundles due to the poor dispersion, which could completely cover the surface of graphene sheets. Meanwhile, these SWNTs bundles also would extend downward from the sheets surface and further contact the underlying graphene sheets to form connections. This dense interlayer distribution leads to excessive contacted sites in the absence of airflow stimulus (Figure S4c,f, Supporting Information). As a result, the change of contact resistance is not as remarkable as expected when the airflow is applied. The inset in Figure 3a also reveals that the three sensors have the sharpest rate of change in current with increasing airflow velocity in the low airflow region (<0.1 m s^{-1}). The highly sensitive response of the hybrid film to minute airflow is similar to the highly sensitive Merkel receptors to low-level airflow and gentle touch.[35] Among them, the current of G_1S_1EM-based sensor varies most significantly with increasing flow rate due to the formation of a relative perfect hybrid structure with a suitable number of interlayered SWNTs microspring structures (Figure S4b,e, Supporting Information). Therefore, it is supposed that the composite strategy can favorably enhance the airflow sensing performance at an appropriate of weight ratios between SWNTs and graphene sheets. When the weight ratio of SWNTs in the composite is too much or too low, the airflow sensing performance is not as excellent as predicted due to the limited variation of the contact sites. The microspring-like microstructure can be achieved via uniformly distributed of SWNTs between the graphene layers, allowing optimal performance of airflow sensors. In the subsequent experiments, the G_1S_1H-based membrane is chosen for the airflow sensor unless otherwise stated.

The setup for testing airflow sensing performance is illustrated in Figure S6, Supporting Information, including a nitrogen tank, glass rotameter, gas mass flowmeter, and GSEM-based airflow sensor. First, the relative current variation in response to airflow at different velocities is explored. Figure 3b shows a typical plot of the relative change in current versus airflow velocity. The airflow direction is perpendicular to the surface of GSEM, and the tube port is less than 5 mm from the sensor surface. The airflow was turned on/off three times continuously at each flow velocity, and the airflow sensor exhibits high resolution and reproducible response curves even at a very low airflow velocity. When the velocity becomes stronger (over 3 m s^{-1}), the top region of the curve is split, probably attributed to the bouncing of the airflow that causes multiple blowing of the GSEM surface. In addition, the current change remains constant at 3.5 and 4 m s^{-1} as the airflow velocity continues to increase (Figure S7, Supporting Information). Therefore, the

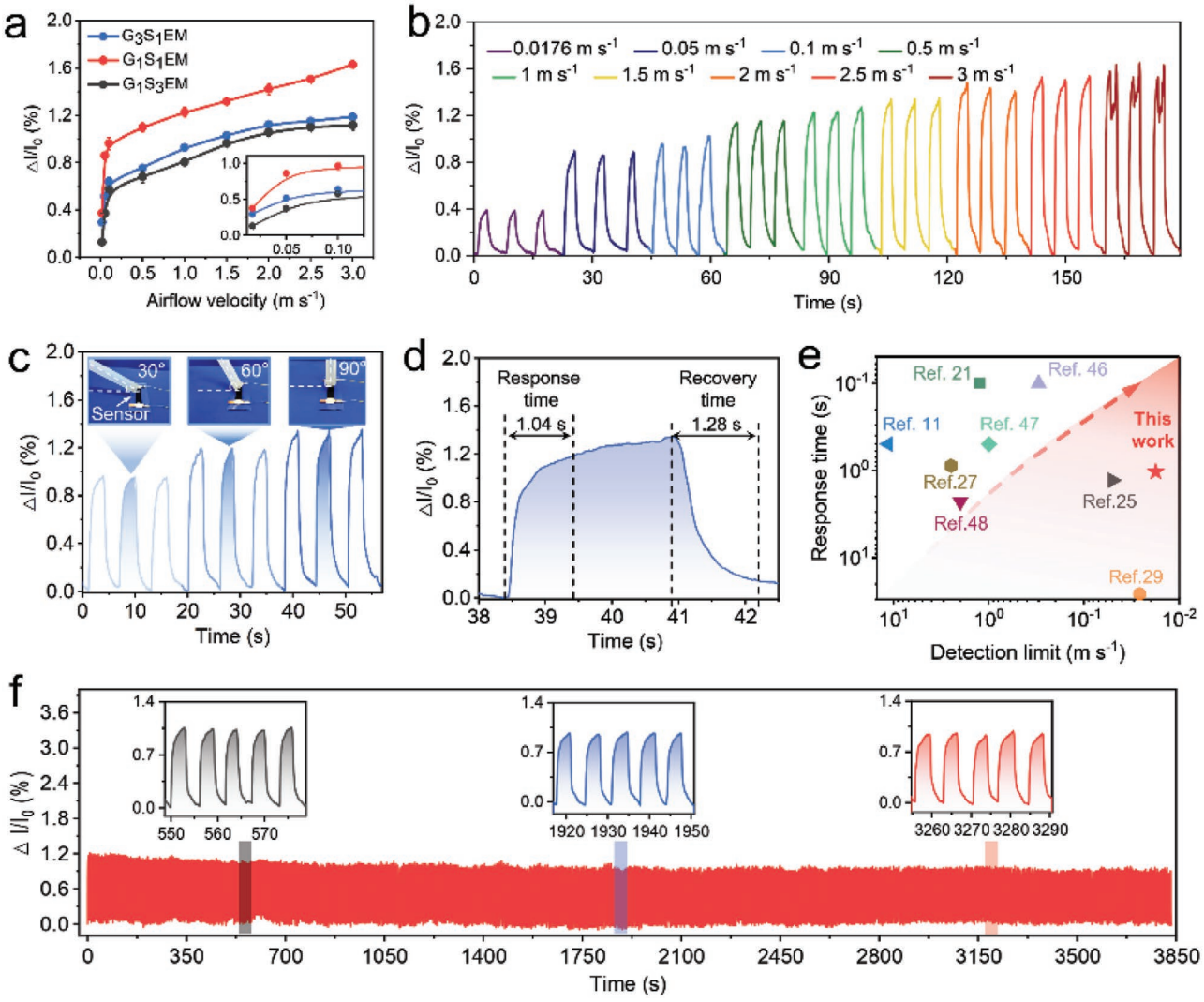

Figure 3. Airflow sensing performance of the GSEM based sensor. a) Plots of the relative current variation versus airflow velocity for airflow sensors based on G_3S_1EM, G_1S_1EM, and G_1S_3EM (*x* and *y* represent the weight ration of Gr and SWNTs in G_xS_y). b) Cyclic curves of relative current variation against airflow velocities based on G_1S_1EM sensor. c) Airflow sensing curves at airflow velocity of 1.5 m s^{-1} with different airflow blowing angles. d) Measurement of response and recovery time from the relative current variation curve. e) Comparison of the detection limit and response time of G_1S_1EM based airflow sensor with other reported airflow sensors in previous works.[11,21,25,27,29,46–48] f) Relative current variation curve of 660 airflow cyclic on/off at the airflow velocity of 1.5 m s^{-1} and blowing angle of 90°.

response range of the GSEM-based airflow sensor is ≈0.0176–3.5 m s^{-1}. The sensitivity *S* of the airflow sensor is defined as the following:

$$S = \frac{\delta\left(\frac{\Delta I}{I_0}\right)}{\delta v} \tag{2}$$

$$\Delta I = I - I_0 \tag{3}$$

where I_0 and I represent the initial current without airflow and the current when airflow is applied, respectively, ΔI is the current variation, and v is the airflow velocity. The sensitivity is calculated based on the slope of the relative current variation curve in Figure S8, Supporting Information, and is divided into two regions: 9.12% m^{-1} s (0.0176–0.1 m s^{-1}) and 0.2% m^{-1} s (0.1–3.5 m s^{-1}). Moreover, the GSEM-based airflow sensor can differentiate airflow with different blow angles. The blowing angle is defined as the angle between the tube and the sensor surface. When the angle changes from 90° to 30°, the relative current variation gradually decreases due to the gradual reduction of the vertical component force of the airflow at the same velocity (Figure 3c). The sensing signal can be detected even when the airflow blowing angle decreases to 0°. However, there is a little noise on the current curve, which may be caused by the low as well as unstable airflow that stimulates vertically on the sensor when the tube is parallel to the GSEM surface. (Figure S9, Supporting Information).

The response and recovery performance of the airflow sensor is investigated in Figure 3d. The response and recovery time are defined as the time from flow on/off to 90% increase/decrease

in relative current variation. Based on the current curve, the response time of the airflow sensor is only 1.04 s at 1.5 m s^{-1} and recovery time is ≈1.28 s, which further confirms the GSEM based airflow sensor is high-sensitive to airflow. Besides, the response and recovery time at other airflow velocities are shown in Figure S10, Supporting Information, where the recovery time is generally slightly longer than the response time. This phenomenon is generally caused by the viscoelasticity of the elastic matrix. Compared with previously reported airflow sensors based on various operating principles, such as thermal, optical, piezoresistive, piezoelectric, electrical, and capacitive principles,[11,21,25,27,29,46–48] the airflow sensor based on contact resistance change in this work performs excellent flow velocity detection limit (0.0176 m s^{-1}) and fast response time (1.04 s) (Figure 3e and Table S1, Supporting Information). Figure 3f demonstrates the sensing signal over 660 consecutive cycles of airflow on/off with no significant current signal drop in the inset, indicating the excellent stability and reliability of the GSEM-based airflow sensor. The superior sensing performance of GSEM-based airflow sensors is inextricably associated with the interface preparation method. To demonstrate the advantages and importance of this interfacial strategy, the performance of the airflow sensor constructed using the bulk mixing method was measured. As shown in Figure S11, Supporting Information, it exhibits low sensitivity and poor signal-to-noise ratio due to the absence of the preformed microspring-like structure.

Benefiting from the ultrathin and flexible characteristic of GSEM, it can be further transferred onto diverse targeted substrates, which can effectively adapt conformally to the smooth or rough surface for favorable self-adaptability. In our system, a flat glass slide, a flexible silicone rubber sheet with an initial bending angle of 38°, a rough stone surface, and the round bottom of a flask are chosen as substrates (**Figure 4**a). The results illustrate that even on the rough stone surfaces, the GSEM can still spread smoothly on the textured surface. The excellent transferability and tight adhesion to the substrate ensure robust sensing performance of the GSEM-based airflow

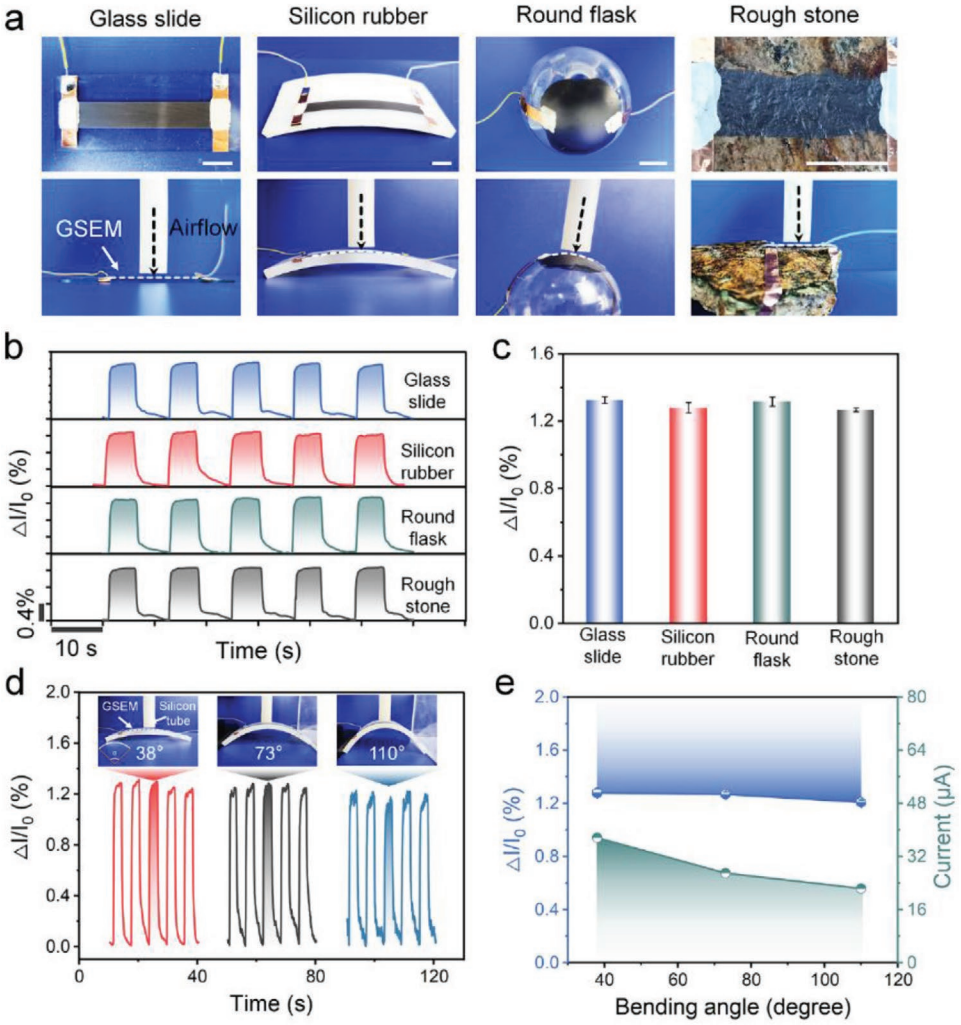

Figure 4. a) Photographs cyclic curves of relative current change and b,c) the specific current variation values when GSEM-sensor is adapted onto different substrates, including flat glass slide, flexible silicon rubber sheet, round-bottom flask and rough stone surface. Scale bar: 1 cm. d) Relative current variation of GSEM under different tensile levels. e) Relationship of relative current variation/initial current versus bending angle.

sensor. The corresponding relative current variation curves for airflow stimulation of 1.5 m s^{-1} are presented in Figure 4b with almost identical current variation value for these airflow sensors built up on those different substrates. The current variation value in Figure 4c more intuitively demonstrates the stability of the airflow sensing performance. Compared with the conventional airflow sensors, the GSEM-based flexible sensors are endowed with good adaptability and can apply to a variety of soft/hard and smooth/rough surfaces without compromising their airflow sensing performance.

In addition, flexible electronics are commonly required to be used in a stretched condition, the GSEM shows excellent stretchability and tensile strength (Figure S12, Supporting Information). The sensing performance of GSEM-based airflow sensors in a tensile state is also measured. The tensile level of GSEM is indicated by the center angle, and the silicon tube located directly above the silicone rubber sheet, where the degree of stretch is the significant. Surprisingly, the GSEM transferred to the flexible silicone rubber sheet could still maintain a relatively stable sensing signal when the silicon sheet is bent from the initial 38° to 73° and 110° (Figure 4d). Additionally, the initial current of GSEM-based sensor gradually dropped with increasing bending angles, which may be the result of the partial disruption of the internal transverse conductive path. When the bending angle reaches 110°, the relative current change value remains almost the same as the initial one (Figure 4e). However, as the bending angle increases to 144°, the relative current variation curve becomes somewhat noisy and the current variation value decreases slightly, which may be attributed to slight damage to the internal microspring structure caused by overstretching of the film (Figure S13, Supporting Information). The above results show that GSEM has favorable structural stability and can maintain excellent airflow sensing performance even in a certain degree of stretching.

Based on the desirable performance of GSEM-based airflow sensor, we further demonstrate its potential application in a smart window system via flow velocity threshold control. People usually would like to open windows on windy and sunny days to keep indoor ventilation, and close windows on windy days to prevent bad weather from affecting indoor environment. The process of opening or closing windows can be intelligently controlled by GSEM-based airflow sensor, thus avoiding the trouble and inconvenience of human operation. As depicted in **Figure 5**a, when the airflow sensor is stimulated by a breeze and outputs a signal with a relative current change below a threshold, the window will automatically remain open. As the wind becomes stronger and the relative current variation of the airflow sensor exceeds the threshold value, the window will close. The components between the airflow sensor and the window are displayed in Figure S14, Supporting Information, which consists of four parts: signal input, signal amplification, signal processing, and signal output. The airflow velocity is controlled by the distance between the silicone tube and the airflow sensor.

As shown in Figure 5b and Movie S1, Supporting Information, in the original state, the tube is so far away from the sensor that the airflow applied to the sensor surface is negligible, and the window remains open. As the tube slowly approaches the sensor, the window suddenly close automatically when the tube reaches a certain distance from the surface of GSEM (State-1). After that, the pipe slowly moves away from the sensor to a certain distance, and the window is opened abruptly due to the low airflow velocity sensed by the sensor (State-2). Thereafter, as the distance continues to increase until the silicon tube is removed away, the window remains open all the time (State-3). The change of current and the tube's distance during one process of opening and closing window is recorded in Figure 5c. In the initial stage, the current change is zero, indicating that the flow rate detected by the airflow sensor is too low, so the window opens. As the tube approaches the sensor, the relative current change gradually increases, and when it is higher than the threshold, the window closes (State-1). As the tube is gradually moved away from the sensor, the relative current change will immediately decrease. The window will not open immediately until the current change is below the threshold (States-2 and 3). Besides, the intelligent open/close process of the smart window was conducted for 55 cycles, which indicates the superior stability and reliability of the GSEM-based airflow sensor in practical application (Figure S15 and Movie S2, Supporting Information). More importantly, the window with on/off state can be controlled at different angles by setting multiple thresholds. As presented in Figure 5d, the relative current variation gradually increases as the tube approaches. The window progressively closes from 45° with an interval of 15° when the current change is in four stages I, II, III, and IV, respectively. When the tube leaves, the window gradually opens from 0° to 45°. This process can also be repeatedly implemented, and the corresponding video is provided in Movie S3, Supporting Information.

Furthermore, the GSEM can be easily cut into desired shapes and integrated into a designable airflow sensors array, enabling to perceive the magnitude and spatial distribution of the airflow stimulus. As a result, a 4 × 4 airflow sensor array is illustrated in **Figure 6**a, which consists four parts: electrode, GSEM, glass slide, and acrylic substrate (Figure 6b). When the airflow is applied vertically on the surface of a sensor, it has the maximal current change. The airflow will spread from the central stimulation site to the surrounding area, so that the neighboring sensors are also stimulated by the airflow and generate sensing electrical signals. If the flow rate becomes higher, the diffusion distance of the airflow will be farther. The sensor is positioned further away from the point of airflow stimulation and the corresponding output current signal is lower. Based on the above principles, the airflow with different velocities and stimulus positions can be distinguished by the 4 × 4 airflow sensor array by comparing the relative current variation value of each sensor (Figure 6c). When the airflow perpendicularly blowing to the sensor located at (2,2) with low velocity, only the sensor at this position exhibits a significant current response. At this time, if the flow rate is increased, the current variation of the airflow sensor located at (2,2) increases, and some of the surrounding sensors will also output obvious sensing signals (Figure S16a,b, Supporting Information). Similarly, when the airflow moves from the top of one sensor to the middle position in the array at the high flow rate, each sensor in the array also exhibits different sensing signals in these two cases, thus achieving the discrimination of the spatial position of the airflow stimulus (Figure S16b,c, Supporting Information).

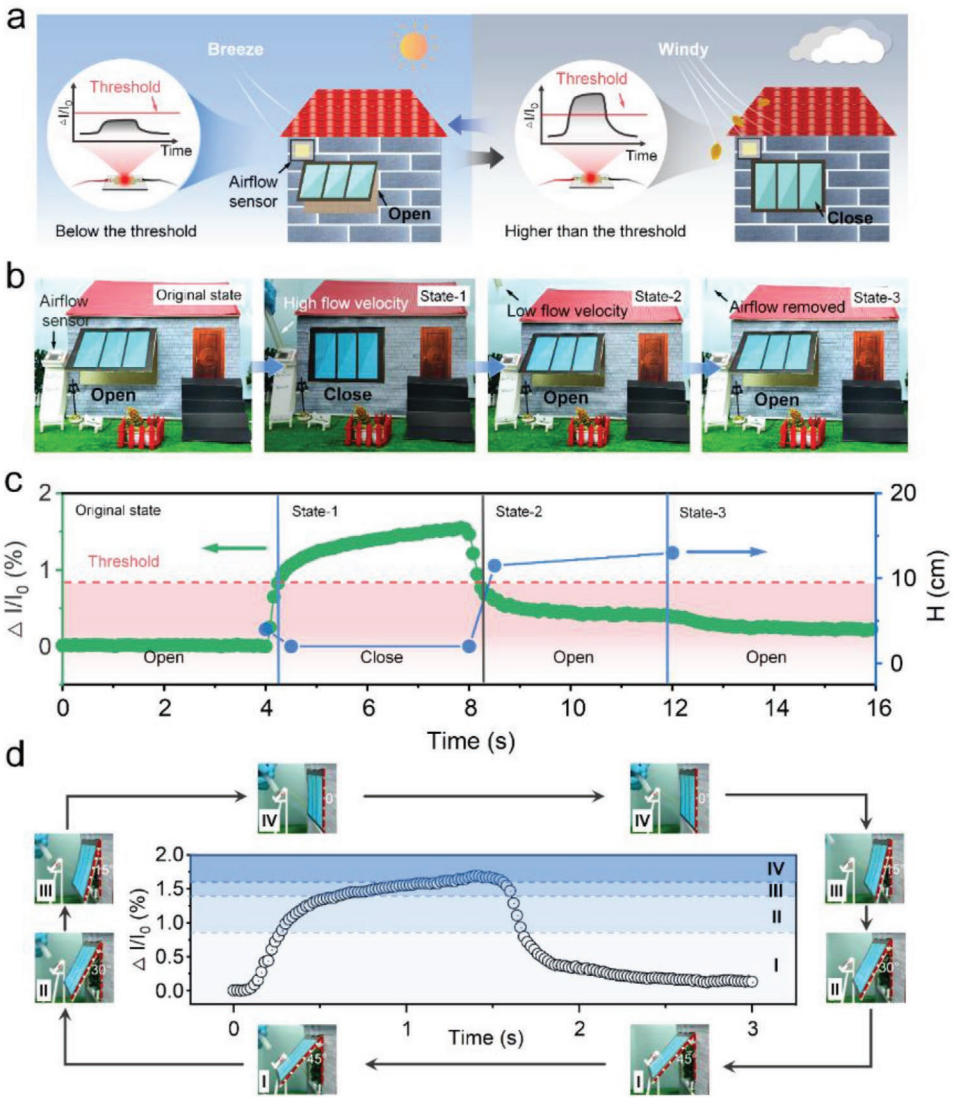

Figure 5. a) Schematic of the smart window open on a breeze day and close on a windy day when the relative current variation of the airflow sensor is below and higher than the threshold, respectively. b) Pictures of the window's state (open or close) at original state, state-1, state-2, and state-3 as the silicon tube slowly approaches and moves away from the sensor. c) The relative variation of current and the tube's distance during one process of opening and closing the window automatically. d) The window was controlled to open and close at different angles by multiple thresholds control.

Owing to the excellent spatial resolution of the airflow sensor array, the motion of a wireless vehicle can be manipulated by an airflow sensor array in a noncontact mode. As depicted in Figure 6d, a 2 × 2 array is built up with four sensors representing the front, back, left, and right directions, respectively. When the airflow blows any of the sensors in the array, the vehicle will move in the corresponding direction. The entire manipulation system is displayed in Figure 6e. When one of the sensors in the array is blown by the airflow, the generated electrical signals are transmitted to four independent amplifiers through a four-wire interface. After that, the amplified signals are transmitted to the Arduino module for processing, and finally the wireless manipulation of the car motion direction is realized via Bluetooth. The circuit diagram and working principle of such a system are illustrated in Figures S17 and S18, Supporting Information, respectively. In brief, when airflow is applied on any of the sensors in the array, there is a maximum change in the corresponding output electrical signal. When its electrical signal exceeds the threshold value and the electrical signals of the other three sensors are below the threshold value, the car moves in the corresponding direction. Figure 6f demonstrates a wireless vehicle being successfully manipulated in noncontact mode by a 2 × 2 airflow array, moving in the front, back, left, and right directions, respectively. The real-time video and electrical signals of the motion process can be found in Movie S4 and Figure S19, Supporting Information, respectively.

3. Conclusion

In summary, inspired by the bats' wing membrane with the unique capability of airflow sensing, we designed a highly

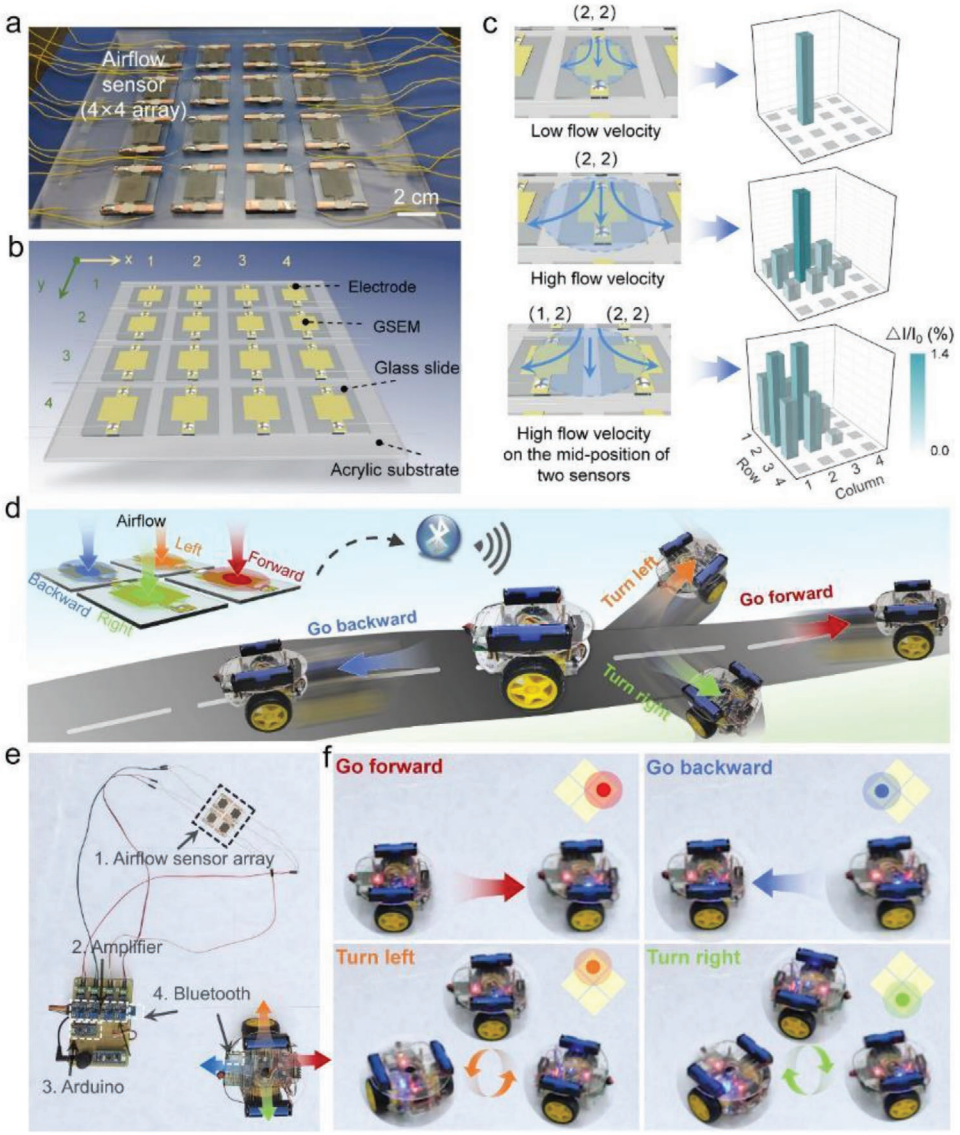

Figure 6. a,b) Photograph and schematic of a 4 × 4 airflow sensor array. c) Differentiation of magnitude and spatial distribution of the airflow stimulus through the 4 × 4 array with airflow applied vertically on the array at a height of 1.5 cm. d) Diagram of a wireless vehicle's motion being manipulated in noncontact mode through a 2 × 2 airflow sensor array. e) The composition part of the noncontact wireless manipulation system. f) Photos of a wireless vehicle being manipulated to go forward, go backward, turn left, and turn right by airflow stimulating the array.

sensitive and adaptive GSEM-based airflow sensor enabled by microspring effect. The GSEM was prepared through interfacial self-assembly of graphene/SWNTs interlayered structures and asymmetric Ecoflex functionalization for a monolithic hybrid membrane. When airflow is applied, the contact resistance among the interlayered SWNTs and graphene sheets can experience a remarkable decrease through spring-like mechanical deformation of interlayered SWNTs. As a result, the flexible airflow sensor shows ultralow airflow velocity detection limit (≈0.0176 m s^{-1}), fast response time (≈1.04 s), wide airflow range (0.0176–3.5 m s^{-1}), and favorable cyclic stability (660 times). As proof of concept, the GSEM based airflow sensor is further introduced into the intelligent home system to realize a wind-threshold-control window switch behaviors of open and close. Besides, a 4 × 4 airflow sensor array was further designed to differentiate the magnitude and spatial distribution of airflow, followed by further manipulation of a wireless vehicle with effective direction control in noncontact mode. The flexible, adaptive monolithic thin membranes enabled by microspring effect are expected to demonstrate significant potentials in flexible electronics and noncontact devices manipulation.

4. Experimental Section

Materials: SWNTs (diameter < 2 nm; length ≈5–30 µm) with purity of over 95% were purchased from Chengdu Organic Chemistry Co., Ltd., and thoroughly rinsed with anhydrous ethanol and dried in a stream of nitrogen before use. The graphene slurry (solid content: 5%) was from Ningbo Institute of Material Technology and Engineering, Chinese Academy of Sciences, and was sealed immediately after use to ensure

that the solid content remains constant. Silicon rubber (Ecoflex 00 50) was purchased from Smooth-on, USA. Other analytical reagent grade solvents and reagents were obtained from Sinopharm Chemical Reagent Co., Ltd. and used as received. Deionized water was used as substrate to prepared GSH film and GSEM at the air/water interface.

Preparation of GSH Film: The GSH film at the water/air interface was prepared according to a previous modified Langmuir–Blodgett assembled method. Typically, pretreated SWNTs (100 mg) and graphene slurry (2000 mg) were dispersed with anhydrous ethanol (200 mL), followed by strong ultrasonication for ≈6 h using an ultrasonic (250 W) to form a uniform and stable dispersion. Subsequently, the resultant dispersion (30 mL) was spread onto the water surface by a spray-coating method, and a uniform pre-assembled film was formed at the water/air interface. After stabilization for ≈30 min, water was rapidly drawn from one side of the water/air interface with a microporous sponge, followed by a significant reduction in the area of the pre-assembled GSH film. Notably, the homogeneous pre-assembled GSH layer was closely packed toward the opposite direction of the siphon situation. When the compression of the film stopped and sponges could not compress the film further, it indicated that the film with dense structure was finally formed. For single graphene and single SWNTs used for comparison, the preparation process was the same as above except for the masses of SWNTs and graphene slurry in the dispersion were different.

Preparation of GSEM: The prepolymer and cross-linker of Ecoflex (1:1, w/w) were diluted using N-heptane with a weight ratio of 5.5%. Then, the obtained mixture solution (35 mL) was dripped onto the surface of the as-prepared GSH film. After curing at room temperature for 6 h, the GSEM was obtained at the water/air interface. For thin membranes using single graphene and SWNTs as sensing layer, the preparation process is the same as above.

Fabrication of GSEM Based Airflow Sensor: GSEM prepared at the water/air interface was transferred onto a glass slide at first. After removing the water and forming a close contact between the film and the glass surface in a 60 °C oven, the GSEM was cut into strip with a size of 0.8 × 5 cm. Then, copper tape was cover on the two ends of the GSEM strip with the aid of sliver paste curing at 60 °C, following by welding aluminum wire to the end of copper tape, thus the electrode was formed and the GSEM based airflow sensor was successfully fabricated.

Fabrication of Airflow Sensor Array: First, the prepared GSEM was transferred to 16 blocks of glass sheets with a size of 2.5 × 3 cm, followed by drying at 60 °C to make the film adhere closely to the glass sheets. Then, all the films were cut into a rectangle with a size of 1.5 × 3 cm, leaving strips with a size of 0.75 × 0.5 cm on both sides of the rectangle for electrodes. After the electrodes were formed, all the films were transferred onto the surface of the PMMA plate with the glass sheet's bottom stuck by double-side tape to form a 4 × 4 airflow sensor array.

Airflow Sensing Performance Test: The current output of the airflow sensor and the array was tested by an electrochemical workstation (CH Instruments, CHI660E.Chenhua Co., Shanghai, China) under a constant initial voltage of 1 V at room temperature. The airflow velocity (v) was calculated by the following formula (4):

$$v = \frac{Q}{S} \tag{4}$$

where Q is the nitrogen's flow flux, read directly from commercial gas mass flowmeter (MF5712) and S is the cross-sectional area of silicone tube measured with a vernier caliper. The flow flux value is adjusted by the valve of the nitrogen tank and the glass rotameter.

Characterization: SEM was performed to observe the micromorphology and structure of undecorated GSH films and GSEM with a Hitachi S4800 cold field emission SEM at an accelerating voltage of 4 kV. Raman spectra were collected by R-3000HR spectrometer (Raman Systems, Inc., R-3000 series) using a solid-state diode laser (532 nm) as an excitation source with a frequency range of 3500–300 cm^{-1}. The tensile performance was conducted by the Zwick Z1.0 universal testing machine. GSEM was cut into rectangular strips (25 × 5 mm) with one end fixed and the other end elongated at a constant rate (50 mm min^{-1}).

Supporting Information

Supporting Information is available from the Wiley Online Library or from the author.

Acknowledgements

W.Z. and P.X. contributed equally to this work. This research was supported by the Natural Science Foundation of China (52073295, 51803226) the Sino-German Mobility Program (M-0424); Key Research Program of Frontier Sciences, Chinese Academy of Sciences (QYZDB-SSWSLH036), Bureau of International Cooperation, Chinese Academy of Sciences (174433KYSB20170061), and K. C. Wong Education Foundation (GJTD-2019-13).

Conflict of Interest

The authors declare no conflict of interest.

Data Availability Statement

Research data are not shared.

Keywords

airflow sensing, microspring effects, monolithic thin-membranes, noncontact manipulation

Received: June 3, 2021
Revised: July 5, 2021
Published online:

[1] A. Chortos, J. Liu, Z. Bao, *Nat. Mater.* **2016**, *15*, 937.
[2] Y. Lee, J. Park, A. Choe, S. Cho, J. Kim, H. Ko, *Adv. Funct. Mater.* **2020**, *30*, 1904523.
[3] Z. Gao, S. Chen, R. Li, Z. Lou, W. Han, K. Jiang, F. Qu, G. Shen, *Nano Energy* **2021**, *86*, 106078.
[4] G. H. Lee, T. M. Choi, B. Kim, S. H. Han, J. M. Lee, S.-H. Kim, *ACS Nano* **2017**, *11*, 11350.
[5] J. An, P. Chen, Z. Wang, A. Berbille, H. Pang, Y. Jiang, T. Jiang, Z. L. Wang, *Adv. Mater.* **2021**, *33*, 2101891.
[6] C. Wan, P. Cai, M. Wang, Y. Qian, W. Huang, X. Chen, *Adv. Mater.* **2020**, *32*, 1902434.
[7] J. He, P. Xiao, W. Lu, J. Shi, L. Zhang, Y. Liang, C. Pan, S.-W. Kuo, T. Chen, *Nano Energy* **2019**, *59*, 422.
[8] J. He, P. Xiao, J. Shi, Y. Liang, W. Lu, Y. Chen, W. Wang, P. Théato, S.-W. Kuo, T. Chen, *Chem. Mater.* **2018**, *30*, 4343.
[9] G. A. Jacobs, J. P. Miller, Z. Aldworth, *J. Exp. Biol.* **2008**, *211*, 1819.
[10] M. E. McConney, C. F. Schaber, M. D. Julian, W. C. Eberhardt, J. A. C. Humphrey, F. G. Barth, V. V. Tsukruk, *J. R. Soc., Interface* **2009**, *6*, 681.
[11] Y.-F. Liu, P. Huang, Y.-Q. Li, Q. Liu, J.-K. Tao, D.-J. Xiong, N. Hu, C. Yan, H. Wang, S.-Y. Fu, *J. Mater. Chem. A* **2019**, *7*, 1889.
[12] J. Tao, X. Yu, *Smart Mater. Struct.* **2012**, *21*, 113001.

[13] T. Jiang, L. Deng, W. Qiu, J. Liang, Y. Wu, Z. Shao, D. Wang, M. Zhang, X. Qian, J. Zhong, X. Wang, L. Lin, *Biosens. Bioelectron.* **2020**, *163*, 112288.
[14] S. A. Araujo-Estrada, F. Salama, C. M. Greatwood, K. T. Wood, T. S. Richardson, S. P. Windsor, in *AIAA Guidance, Navigation, and Control Conf.*, American Institute of Aeronautics and Astronautics, Grapevine, Texas **2017**.
[15] R.-H. Ma, Y.-H. Wang, C.-Y. Lee, *Sensors* **2011**, *11*, 2715.
[16] H. W. Wu, A. D. S. Gillies, in *Eighth Int. Mine Ventilation Congress*, (Ed: A. D. S. Gillies), The Australasian Institute of Mining and Metallurgy, Australia **2005**, 7.
[17] M. M. Sadeghi, R. L. Peterson, K. Najafi, *J. Micromech. Microeng.* **2013**, *23*, 085017.
[18] H.-B. Liu, N. Lin, S.-S. Pan, J. Miao, L. K. Norford, *IEEE Sens. J.* **2013**, *13*, 1914.
[19] F. Xing, G.-X. Meng, Q. Zhang, L.-T. Pan, P. Wang, Z.-B. Liu, W.-S. Jiang, Y. Chen, J.-G. Tian, *Nano Lett.* **2014**, *14*, 3563.
[20] A. Talbi, L. Gimeno, J.-C. Gerbedoen, R. Viard, A. Soltani, V. Mortet, V. Preobrazhensky, A. Merlen, P. Pernod, *J. Micromech. Microeng.* **2015**, *25*, 125029.
[21] K. Takei, Z. Yu, M. Zheng, H. Ota, T. Takahashi, A. Javey, *Proc. Natl. Acad. Sci. U. S. A.* **2014**, *111*, 1703.
[22] P. Nie, R. Wang, X. Xu, Y. Cheng, X. Wang, L. Shi, J. Sun, *ACS Appl. Mater. Interfaces* **2017**, *9*, 14911.
[23] Y. Lee, J. Park, S. Cho, Y.-E. Shin, H. Lee, J. Kim, J. Myoung, S. Cho, S. Kang, C. Baig, H. Ko, *ACS Nano* **2018**, *12*, 4045.
[24] S. Chun, W. Son, C. Choi, H. Min, J. Kim, H. J. Lee, D. Kim, C. Kim, J. Koh, C. Pang, *ACS Appl. Mater. Interfaces* **2019**, *11*, 13608.
[25] H. Wang, S. Li, Y. Wang, H. Wang, X. Shen, M. Zhang, H. Lu, M. He, Y. Zhang, *Adv. Mater.* **2020**, *32*, 1908214.
[26] N. Izadi, M. J. de Boer, J. W. Berenschot, G. J. M. Krijnen, *J. Micromech. Microeng.* **2010**, *20*, 085041.
[27] Y. Bian, R. Liu, S. Hui, *Funct. Mater. Lett.* **2016**, *09*, 1650001.
[28] Y. Bian, Y. Zhang, X. Xia, *J. Bionic Eng.* **2016**, *13*, 416.
[29] Z. Xu, K. Wu, S. Zhang, Y. Meng, H. Li, L. Li, *Mater. Horiz.* **2017**, *4*, 383.
[30] J. Paek, J. Kim, *Nat. Commun.* **2014**, *5*, 3324.
[31] A. Alfadhel, B. Li, A. Zaher, O. Yassine, J. Kosel, *Lab Chip* **2014**, *14*, 4362.
[32] J. Zhang, L. Hao, F. Yang, W. Jiao, W. Liu, Y. Li, R. Wang, X. He, *ACS Appl. Mater. Interfaces* **2016**, *8*, 33848.
[33] K. A. Holbrook, G. F. Odland, *J. Anat.* **1978**, *126*, 21.
[34] S. J. Sterbing-D'Angelo, M. Chadha, K. L. Marshall, C. F. Moss, *J. Neurophysiol.* **2016**, *117*, 705.
[35] S. Sterbing-D'Angelo, M. Chadha, C. Chiu, B. Falk, W. Xian, J. Barcelo, J. M. Zook, C. F. Moss, *Proc. Natl. Acad. Sci. U. S. A.* **2011**, *108*, 11291.
[36] K. L. Marshall, M. Chadha, L. A. deSouza, S. J. Sterbing-D'Angelo, C. F. Moss, E. A. Lumpkin, *Cell Rep.* **2015**, *11*, 851.
[37] P. Xiao, Y. Liang, J. He, L. Zhang, S. Wang, J. Gu, J. Zhang, Y. Huang, S.-W. Kuo, T. Chen, *ACS Nano* **2019**, *13*, 4368.
[38] Y. Liang, P. Xiao, F. Ni, L. Zhang, T. Zhang, S. Wang, W. Zhou, W. Lu, S.-W. Kuo, T. Chen, *Nano Energy* **2021**, *81*, 105617.
[39] S. Wang, Y. Gao, A. Wei, P. Xiao, Y. Liang, W. Lu, C. Chen, C. Zhang, G. Yang, H. Yao, T. Chen, *Nat. Commun.* **2020**, *11*, 4359.
[40] P. Xiao, J. He, F. Ni, C. Zhang, Y. Liang, W. Zhou, J. Gu, J. Xia, S.-W. Kuo, T. Chen, *Nano Energy* **2020**, *68*, 104385.
[41] P. Xiao, J. Gu, C. Wan, S. Wang, J. He, J. Zhang, Y. Huang, S.-W. Kuo, T. Chen, *Chem. Mater.* **2016**, *28*, 7125.
[42] A. Cao, P. L. Dickrell, W. G. Sawyer, M. N. Ghasemi-Nejhad, P. M. Ajayan, *Science* **2005**, *310*, 1307.
[43] J. Suhr, P. Victor, L. Ci, S. Sreekala, X. Zhang, O. Nalamasu, P. M. Ajayan, *Nat. Nanotechnol.* **2007**, *2*, 417.
[44] M. R. Falvo, G. J. Clary, R. M. T. Ii, V. Chi, F. P. B. Jr, S. Washburn, R. Superfine, *Nature* **1997**, *389*, 582.
[45] C. Chen, Z. Xu, *Nanoscale* **2011**, *3*, 4383.
[46] S. Zhao, R. Zhu, *Adv. Mater.* **2017**, *29*, 1606151.
[47] J. Park, Y. Lee, J. Hong, M. Ha, Y.-D. Jung, H. Lim, S. Y. Kim, H. Ko, *ACS Nano* **2014**, *8*, 4689.
[48] H. Takahashi, A. Nakai, I. Shimoyama, *Sens. Actuators, A* **2018**, *281*, 243.